Use of Gaussian Type Functions for Describing Fast Ion-Matter Irradiation with Time-Dependent Density Functional Theory

Rika Tandiana, Karwan Ali Omar, Eleonora Luppi, Fabien Cailliez, Nguyen-Thi Van-Oanh, Carine Clavaguéra, Aurélien de la Lande

Use of Gaussian Type Functions for Describing Fast Ion-Matter Irradiation with Time-Dependent Density Functional Theory

Rika Tandiana[1], Karwan Ali Omar[1,2], Eleonora Luppi[3], Fabien Cailliez[1],

Nguyen-Thi Van-Oanh[1], Carine Clavaguéra[1]*, Aurélien de la Lande[1]*

1) Institut de Chimie Physique, Université Paris-Saclay, CNRS, 15 avenue Jean Perrin, F-91405 Orsay, France

2) Department of Chemistry, College of Education, University of Sulaimani, 41005, Kurdistan, Iraq.

3) Laboratoire de Chimie Théorique, Sorbonne Université and CNRS, F-75005 Paris, France

*To whom correspondence should be addressed: carine.clavaguera@universite-paris-saclay.fr, aurelien.de-la-lande@universite-paris-saclay.fr

ABSTRACT

The electronic stopping power is an observable that quantifies the ability of swift ions penetrating matter to transfer energy to the electron cloud. The recent literature has proven the value of Real-Time Time-Dependent Density Functional Theory to accurately evaluate this property from first-principles but questions remain regarding the capability of computer codes relying on atom-centered basis functions to capture the physics at play. In this article, we draw attention to the fact that irradiation by swift ions triggers electron emission into the continuum, especially at the Bragg peak. We investigate the ability of Gaussian atomic orbitals (AOC), that were fitted to mimic continuum wave functions, in improving electronic stopping power predictions. AOC are added to standard correlation-consistent basis sets or STO minimal basis sets. Our benchmarks on water irradiation by fast protons clearly advocate for the use of AOC, especially near the Bragg peak. We show that AOC only need to be placed on the molecules struck by the ion. The number of AOC that are added to the usual basis set is relatively small compared to the total number of atomic orbitals, making the use of such basis set an excellent choice from a computational cost point of view. The optimum basis set combination is applied for the calculation of stopping power of a proton in water with encouraging agreement with experimental data.

1. INTRODUCTION

The interaction of high energy, ionizing, radiations (*e.g.* X, extreme UV, XUV or γ photons, fast ions or electrons) with matter is of major importance in various scientific contexts. In medicine for instance, swift ions (*e.g.* H^+ or C^{6+}) and X photons are used for the treatment of cancers in radiotherapies[1]. In space, on the other hand, the chemistry that takes place on dusts[2,3] or in the atmosphere of Jovian planet's satellites are thought to be modulated by collisions with high energy particles from the sun or from the cosmos[4,5]. As a final example, we mention the nuclear industry, for which the question of corrosion inside a nuclear plant reactor or the extraction of degradation effluents, are both central for safety reasons and for the longevity of nuclear installations [6].

The mechanisms of energy deposition in matter by fast ions, together with the first relaxation decays, govern the production of electron-hole and of charge migrations (electron cloud dynamics). These early steps condition all the subsequent phenomena that eventually lead to chemical alterations of irradiated matter. Energy deposition in ion-matter irradiation is quantified by the stopping power. At the microscopic level, it is defined as $S \equiv -\partial E_k / \partial r_{prj}$, that is the derivative of the projectile's kinetic energy with respect to its infinitesimal displacement. As ions interact with both electrons and atom nuclei, S can be separated into a nuclear contribution (S_n), an electronic contribution (S_e) and eventually an electronic/nuclear coupling term $S_{n/e}$[7]. For ions with kinetic energy of a few tens of keV to a few MeV, S_e largely dominates over S_n and only the former will be of interest here. Typical profiles of S_e as a function of the projectile's kinetic energy on the 10 keV-MeV range are non-monotonic, first increasing with the projectiles' speed, up to a maximum called the Bragg peak, then decreasing for higher kinetic energies. The elaboration of theoretical models aiming at rationalizing stopping power has a long history[8]. These models are for example used in semi-empirical Monte Carlo track structure codes[9]. The advent of sophisticated quantum chemistry approaches and powerful supercomputers have opened the door toward the evaluation of stopping power from first principles.

Notably, Density Functional Theory (DFT)[10,11] and its Time-Dependent version (TD-DFT)[12,13] are particularly suited to tackle the dynamics triggered in the electron cloud by ionizing radiation[14]. The appeal of DFT and TD-DFT is the combination of accuracy and computational efficiency that enables simulations of very large molecular systems[15–17]. Researchers have examined the ability of TD-DFT to calculate S_e, in particular via the so-called Real-Time TD-DFT approach (RT-TD-DFT) that consists in the explicit propagation in time of the electronic equations-of-motion[18]. So far, applications of RT-TD-DFT for S_e evaluations are encouraging[18–21], even though important aspects remain to be clarified, in particular regarding the mathematical choice that must be made in order to represent the electronic wave functions. Using plane wave codes, Correa and coll. and Kanai and coll. showed that S_e can be

reliably evaluated from RT-TD-DFT simulations over a wide range of projectile's kinetic energies, including the Bragg peak region [16,22–28], thereby showing the ability of plane-waves to properly describe associated wave functions. The situation is, to our point of view, less clear when using Gaussian basis functions. On one hand, Artacho and co-workers evaluated S_e for proton and alpha particle in Au, Al and LiF for low kinetic energies, *i.e*. below the Bragg peak, with good agreement with available experiments[18,29,30]. On the other hand, Bruneval and co-workers reported a great sensitivity of the calculated S_e with the basis set via thoughtful benchmarks for S_e in lithium and aluminum[31,32] for projectile's kinetic energy ranging from 0.01 MeV to 1 MeV. To optimize the basis set choice, they proposed a trial-and-error approach to build *ad hoc* basis sets for S_e calculations including the basis functions within the Dunning series that mostly influence the stopping power value. A drawback of the approach seems to be the generation of rather large basis sets, hence computationally expensive to ensure convergence of the calculated stopping power. More recently, calculations of electronic stopping power for proton in water was reported by Artacho, Kohanoff and co-workers[19]. Provided adequate sampling of ion-water molecule irradiation conditions, the authors were able to recover the experimental stopping power curve. We note that here again, a rather large split-valence triple-zeta basis set was used on all atoms (6-311G**(2d,2p)). In summary, while previous studies have established the reliability of RT-TD-DFT for *ab initio* calculations of electronic stopping power, and even the coupled $S_{n/e}$ terms[7], the conditions for which Gaussian function basis codes can achieve the same performances as plane-wave codes remain unclear. From recent literature, it transpires that large, hence computationally expensive, Gaussian basis sets are mandatory in order to converge the simulated properties.

Plane-waves can achieve remarkable accuracy over the entire simulation boxes provided sufficiently large cutoff values are used. This is for instance necessary to account for core electrons excitations. Moreover, the eventual inclusion of exact exchange contributions to the exchange-correlation potential can turn intractable. Gaussian basis functions are of more flexible use. They can afford exchange-correlation functionals with fractions of exact exchange at manageable cost. In conclusion, it is thus worthwhile to pursue both kinds of methods for radiation chemistry problems.

Here, we propose a less computationally costly approach that explicitly includes, with Gaussian basis sets, the physics of the process we want to describe. Indeed, a characteristic of excitations caused by fast ion collisions is the emission of electrons in the continuum or in conduction bands, the wave functions of which exhibit several nodes and fast oscillations. This is particularly true near the Bragg peak where energy deposition is the highest. This characteristic feature has so far not been fully appreciated in our point of view. We make the hypothesis that the S_e underestimation with Gaussian basis sets comes from a poor description of the high-lying excited states and, in particular, of the

continuum states that are involved in these electronic excitations. In fact, the high energy states are usually very poorly described with standard Gaussian basis sets, and the correct nodal structure (continuum oscillatory behavior) of the wavefunction is not reproduced[33].

In the literature some strategies have been proposed to improve Gaussian basis sets to describe high lying excited and continuum states. Kaufmann *et al*.[34] and more recently, Wozniak *et al*.[35] proposed a fitting procedure able to optimally represent Rydberg and continuum energy states of atoms in Gaussian basis sets. A different approach to obtain Gaussians optimized for the continuum was proposed in the context of electron–molecule scattering by Nestmann and Peyerimhoff[36] for neutral systems. The method has been further extended by Faure *et al*. [37] for the description of charged systems, such as ions. These Gaussian-type-orbitals have been used for example in cross-sections calculations for electron- or positrons molecules collisions via the "R-matrix" approach[38–40]. The use of Gaussians specific to describe the high lying excited states and the continuum has been demonstrated to be fundamental to correctly describe physical processes involving specifically these types of energy states[41]. The generated basis sets have been applied for calculations of bound and continuum states of charged molecules, such as C_nH^- and N_2^+.

In this article we investigate the capability of atomic orbitals optimized for the continuum generated by the procedure of Nestmann and Peyerimhoff[36] in the context of S_e calculation. We consider proton penetration in water and report extensive benchmarks. We show remarkable improvement of calculated electronic stopping power values at a very reasonable computational price. The results analyses permit to better understand the phenomena at play in fast ion-matter irradiation.

2. Gaussian type orbitals for the continuum

2.1 Fitting parameters

Nestmann and Peyerimhoff [36] and later Faure *et al*.[37] developed a method and a computational code (GTOBAS and NUMCBAS) which are able to construct adequate Gaussian-type-orbitals continuum basis sets for representing numerical continuum orbitals (u_{hl}) over a finite range. l is the second quantum number. The functions u_{hl} are determined over grid points r_k by solving a single channel scattering equation with the NUMCBAS module. At this stage, the effective charge of the scattering process's target, which defined the model potential is specified, together with the boundary radius (R) and an upper energy bound (E). The optimization of the exponents of Gaussian functions (α_i) to fit continuum functions (u_{hl}) is then achieved with GTOBAS by minimizing the following $F_{l,N}$ function,

$$F_{l,N} = \sum_{h=1}^{N} \frac{\sum_k \left[\sum_{i=1}^{n} c_{hi} r_k^l \exp\left(-\alpha_i r_k^2\right) - u_{hl}(r_k)\right]^2}{\sum_k [u_{hl}(r_k)]^2} + D(\alpha_1, \dots, \alpha_n) \quad (1)$$

$$D(\alpha_1, \dots, \alpha_n) = \sum_{i=2}^{n} \sum_{j=1}^{i-1} \exp\left(-Rx \left|\frac{\alpha_i}{\alpha_j} - \frac{\alpha_j}{\alpha_i}\right|\right) \quad (2)$$

with N being the number of continuum functions and n the number of Gaussian exponents. The coefficients c_{hi} are determined by a least-squared fit. The D function is added to avoid the α_i coefficients to collapse to the same value and to avoid linear dependency issues.

In our calculations, we fitted the continuum orbitals with Coulomb functions. In the following we will indicate these optimal continuum exponents as Atomic Orbitals fitting the Continuum (AOC). We have generated a series of continuum basis sets for neutral H and O atoms separately, varying the boundary radius R, between 3, 4, 8, and 12 bohr, while keeping the upper bound eigenvalues E to 3 or 5 Ry. We have also carried out different calculations changing l between 2, 3 and 4. The list of generated exponents can be found in Table 1 for two sets of AOC. As can be seen from the exponents reported in the Table, the AOC are not especially diffuse, and actually also contain rather contracted basis functions.

Table 1: three atomic orbital basis sets for the continuum generated with the GTOBAS program for hydrogen and oxygen. A contraction degree of one is used for all functions. L refers to the maximum second quantum number of the set. The exponents are given in bohr^{-2}.

	R3-L2-E5		R3-L3-E5
L	H	O	O
s	1.710454	43.427950	42.804237
	0.123936	1.248411	1.007852
	0.029705	0.441522	0.430483
		0.141377	0.173415
		0.039096	0.062317
p	0.552411	23.750649	7.237503
		4.098560	0.823115
		0.980036	0.387840
		0.333144	0.171542
		0.100335	0.067076
d	0.552411	7.053886	6.326432
		1.733890	1.556423
		0.458709	0.585402
		0.112128	0.249634
		0.023529	0.097136
f			2.797851
			0.866865

The exponents we obtained from the fitting are specific for the description of the continuum states. Therefore, in order to obtain a well-balanced Gaussian basis sets, we completed the AOC with Dunning type of basis[42–45] that we imported from the Basis Set Exchange library[46].

2.2 Computational details

We now investigate the performance of AOC enriched basis sets for the prediction of electronic stopping power curves. To this end, we have considered twelve water slabs comprised of ca. 50 water molecules that we irradiate with fast protons (hereafter referred to as the projectile) traveling along the z-axis (Figure 1). The Cartesian coordinates of the slabs were extracted from classical molecular dynamics simulations. Following the suggestion of Maliyov *et al.* [31] we apply a mixed-basis-set scheme, differentiating water molecules lying close to the projectile's propagation line from the others. They are hereafter named as water$_{close}$ and water$_{far}$ respectively (Figure 1). As soon as an oxygen water atom lies within less than 2.6 Å from the projectile's propagation track, the whole water molecule falls in the water$_{close}$ class. The different combinations of basis sets are summarized in Table 2. We use the generic notation FX-CY to indicate the standard basis set used for bound electrons. FX and CY are respectively a simplified notation for the water$_{far}$ and water$_{close}$ atoms respectively. X and Y indicate the level of valence splitting for the oxygens, namely 2, 3, 4 … for double, triple, quadruple … zeta quality basis sets. In general we use cc-pVDZ on hydrogens, therefore this information is not included in our "FX-CY" style notation. For example, F4-C6 indicates the use of cc-pVQZ on water$_{far}$ oxygens, cc-pV6Z on water$_{close}$ oxygen atoms and cc-pVDZ on all hydrogen atoms. When AOC functions are added (on water$_{close}$ atoms), two triplets of integers a, b and c are added in parentheses for oxygen and hydrogen atoms respectively. a, b, and c are respectively the R value in Bohr, the maximum second quantum number L_{max} and the upper bound eigenvalues in Ry (see above). For example, F2-C3(3.3.5/3.2.5) means that we use cc-pVDZ on water$_{far}$ oxygen atoms, cc-pVTZ on water$_{close}$ oxygen atoms and cc-pVDZ on all hydrogen atoms. For the water$_{close}$ molecules, we add a set of AOC fitted with $R = 3$ bohr, $L_{max} = 3$ and $E = 5$ Ry for oxygens and a set of AOC fitted with $R = 3$ bohr, $L_{max} = 2$ and $E = 5$ Ry for hydrogens. Finally, in some specific combinations, the labels 'aug', 'min', 'ryd' and 'cor' are added. They respectively indicate the addition of diffuse functions, the use of a minimal basis set, the addition of Rydberg functions, or the use of tight core orbitals. The reader is referred to Table 2 for the precise definition of each basis set combination.

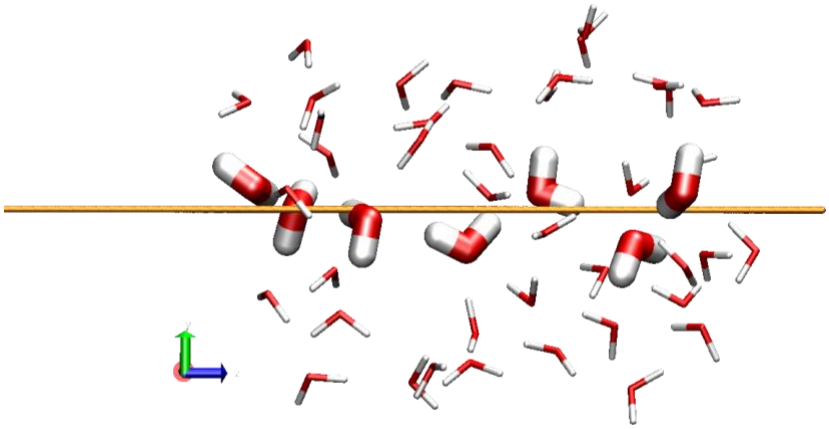

Figure 1: a water slab traversed by a fast proton travelling along the orange line. The water molecules that lie close (< 2.6 Å) to the propagation line (water$_{close}$ *) are represented with thick chemical bonds. The other water molecules (water*$_{far}$) are shown with thin licorice representation. *The color code of the Cartesian coordinated system is as follow: x-axis in red, y-axis in green and z-axis in blue.*

Table 2: basis set combinations considered in this article to investigate the sensitivity of electronic stopping power calculations. N_{AO} *is the number of atomic orbitals in the case of the water slab showed in Figure 1 .* The aug, min, ryd and cor labels indicate the addition of diffusion functions, the use of minimal basis set, the addition of Rydberg functions or the use of tigh core orbitals.

	N_{AO}	water$_{far}$		water$_{close}$	
		O	H	O	H
F2-C2	1175	cc-pVDZ	cc-pVDZ	cc-pVDZ	cc-pVDZ
F2-C3	1315	cc-pVDZ	cc-pVDZ	cc-pVTZ	cc-pVDZ
F3-C4	2360	cc-pVTZ	cc-pVDZ	cc-pVQZ	cc-pVDZ
F4-C5	4152	cc-pVQZ	cc-pVDZ	cc-pV5Z	cc-pVDZ
F4-C6	4740	cc-pVQZ	cc-pVDZ	cc-pV6Z	cc-pVDZ
F2-C6	2540	cc-pVDZ	cc-pVDZ	cc-pV6Z	cc-pVDZ
F2-C2(3.2.5/3.2.5)	1693	cc-pVDZ	cc-pVDZ	cc-pVDZ-R3-L2-E5	cc-pVDZ-R3-L2-E5
F2-C3(3.2.5/3.2.5)	1833	cc-pVDZ	cc-pVDZ	cc-PVTZ-R3-L2-E5	cc-pVDZ-R3-L2-E5
F2-C2(3.3.5/3.2.5)	2043	cc-pVDZ	cc-pVDZ	cc-pVDZ-R3-L3-E5	cc-pVDZ-R3-L2-E5
F2-C3(3.3.5/3.2.5)	2183	cc-pVDZ	cc-pVDZ	cc-PVTZ-R3-L3-E5	cc-pVDZ-R3-L2-E5
F2-C2(8.2.5/8.2.5)	1959	cc-pVDZ	cc-pVDZ	cc-pVDZ-R8-L2-E5	cc-pVDZ-R8-L2-E5
F2-C2(12.2.5/12.2.5)	2274	cc-pVDZ	cc-pVDZ	cc-pVDZ-R12-L2-E5	cc-pVDZ-R12-L2-E5
F2-C2(3.4.5/3.2.5)	2183	cc-pVDZ	cc-pVDZ	cc-pVDZ-R3-L4-E5	cc-pVDZ-R3-L2-E5
F2-C2(3.3.5/4.3.3)	2575	cc-pVDZ	cc-pVDZ	cc-pVDZ-R3-L3-E5	cc-pVDZ-R4-L3-E3
F2-C4(3.3.5/4.3.3)	2960	cc-pVDZ	cc-pVDZ	cc-pVQZ-R3-L3-5	cc-pVDZ-R4-L3-E3
F2-Caug2(3.3.5/4.3.3)	2645	cc-pVDZ	cc-pVDZ	aug-cc-pVDZ-R3-L3-5	cc-pVDZ-R4-L3-E3
Fmin-Cmin(3.3.5/3.2.5)	1239	STO-3G	STO-3G	STO-3G-R3-L3-E5	STO-3G-R3-L2-E5
F2-Cryd2(3.3.5/3.2.5)	2330	cc-pVDZ	cc-pVDZ	DZP-RDH-R3-L3-E5	cc-pVDZ-R3-L2-E5
F2-Ccor2(3.3.5/4.3.3)		DZVP-GGA	DZVP-GGA	cc-pCVDZ-R3-L3-E5	cc-pVDZ-R4-L3-E3

All simulations have been carried out with our multi-GPU implementation of RT-TD-DFT in the deMon2k code (version 6.1.6) using 4 GPU and 40 CPU or 8 GPU and 64 CPU[47]. For electronic integral calculations, we used a mixed scheme for electronic repulsion and adaptive grids of high accuracy for the exchange-correlation contributions (10^{-7} Ha, following deMon2k nomenclature)[48,49]. deMon2k relies on the auxiliary DFT formalism (ADFT) whereby variationally fitted electron densities are introduced to avoid cumbersome four-index electronic-repulsion-integral calculations and to simplify the numerical integration of XC contributions. The extension of ADFT to Real-Time Time-Dependent ADFT was previously shown to be robust and accurate. We refer the reader to recent reviews for more details on the RT-TD-ADFT formalism[50,51]. We have used the automatically generated GEN-A2 auxiliary basis set to expand the auxiliary electronic densities. The auxiliary sets are automatically built from the atomic orbital basis set to span the space covered by the latter. We previously showed that GEN-A2 is reliable to evaluate S_e with deviations of less than 10^{-4} Ha/bohr compared to more complete auxiliary basis sets[52]. We chose Dirac exchange and Vosko, Wilk and Nusair correlation functionals. We do not expect significant influence from the choice of the XC functional on basis set effects[32]. For each water slab, we first obtained the ground state electronic densities by means of a self-consistent-field calculation with tight convergence criteria (10^{-10} Ha and 5.10^{-7} Ha on the electronic energy and density fitting error). The SCF procedure was conducted in absence of the projectile. The projectile was then placed 50 Å away from the molecular system, defining by convention time zero of the RT-TD-ADFT simulation. The projectile is defined as a +1 point-charge generating a Liénard-Wierchet Coulomb potential[53]. No basis functions are placed on the projectile. Electronic dynamics simulations were carried out with a time step of 0.001 fs using a second-order Magnus propagator coupled to a predictor-corrector scheme[52,54]. The matrix exponent entering the propagator expression was evaluated with a Taylor expansion comprising 65 terms. The simulations were terminated when the projectile had traveled 10 Å after traversing the slab. We considered the following projectile kinetic energies to build stopping power curves: 0.001, 0.025, 0.05, 0.075, 0.1, 0.2, 0.3, 0.5, 0.6, 0.7, 0.8 and 1 MeV. For each kinetic energy, we simulated irradiation considering each of the 12 water slabs. We report on Figures 4 to 7 the average stopping power value over each the 12 slabs. For each kinetic energy the statistical uncertainty is estimated via the Student law as $\pm 2.179 * \sqrt{u^2/12}$ where u^2 is the variance of the stopping power calculated over the 12 slabs.

Simulation data were analyzed with the R package for statistical computing and the Rstudio graphical interface [55]. The R studio scripts written to generate Figures together with the data files generated by deMon2k can be downloaded on the Zenodo repository databank (DOI: 10.5281/zenodo.8037349). It is thus possible for an interested user to redraw automatically all the Figures presented in this article, or to conduct complementary analyses based on our data.

2.3 Mechanism of energy deposition

To illustrate the mechanism of electronic excitation caused by fast ions irradiation, we show in Figure 2 and in Fig. S1. the Kohn-Sham MO populations as a function of time. We have chosen one water slab to make these calculations. The line shape was obtained defining, for each MO, a Lorentzian function with 0. 2 eV full-width-at-half-maximum and scaled by its population variation with respect to the ground state. Blue region means depopulation of the orbitals while the orange colors mean the population of initially unoccupied MO. The functions have been renormalized to allow comparisons among the graph. We consider four basis set combinations, namely F2-C2, F2-C3, F2-C6 and F2-C2(3.3.5/4.3.3) and three proton's kinetic energy (0.075, 0.5 and 1 MeV). The vertical blue curves represent the density-of-state (DOS) for each basis set. The stacked black lines on the left represent the energy positions of Kohn-Sham molecular orbitals with the frontier MOs highlighted in color.

The DOS for the F2-C2, F2-C3 and F2-C6, continuously becomes denser above zero. We still note energy regions of lower DOS, notably around 10 eV, and 20 eV with F2-C2, and marked DOS fluctuations up-to 50eV. With F2-C2 or F2-C3 the DOS continuously decays above 30eV. The addition of AOC on the F2-C2 basis set, makes the DOS much denser which always remains above 10 eV^{-1} in the [0-50] eV region. This clearly indicates the improvement of the continuum description with AOC. It is now interesting to have a look at the regions of the energy spectra involved in the excitation. Taking F2-C2(3.3.5/4.3.3) as reference, we see that the excitation process involves all valence electrons that populate initially unoccupied MOs over a wide energy window. For example, at 0.075 MeV, significant electronic populations up to 50 eV are seen with a pick around 5 eV. Comparing the excitations patterns at higher kinetic energies (0.5 and 1 eV), we note a similar mechanism, although with less energetic excitations.

The situation is more contrasted with basis set deprived from AOC functions. With the F2-C6 basis set, the general view is preserved although the decay of electronic excitations above 5eV is less smooth than with F2-C2(3.3.5/4.3.3). On the other hand, with F2-C2 and F2-C3, we clearly see white areas in the excitation spectra, notably around 10 and 20 eV or above 40 eV with F2-C2. This is clearly to be related to the smaller DOS at these energies. In the following sections, we examine the consequences of these features on the electronic stopping power values.

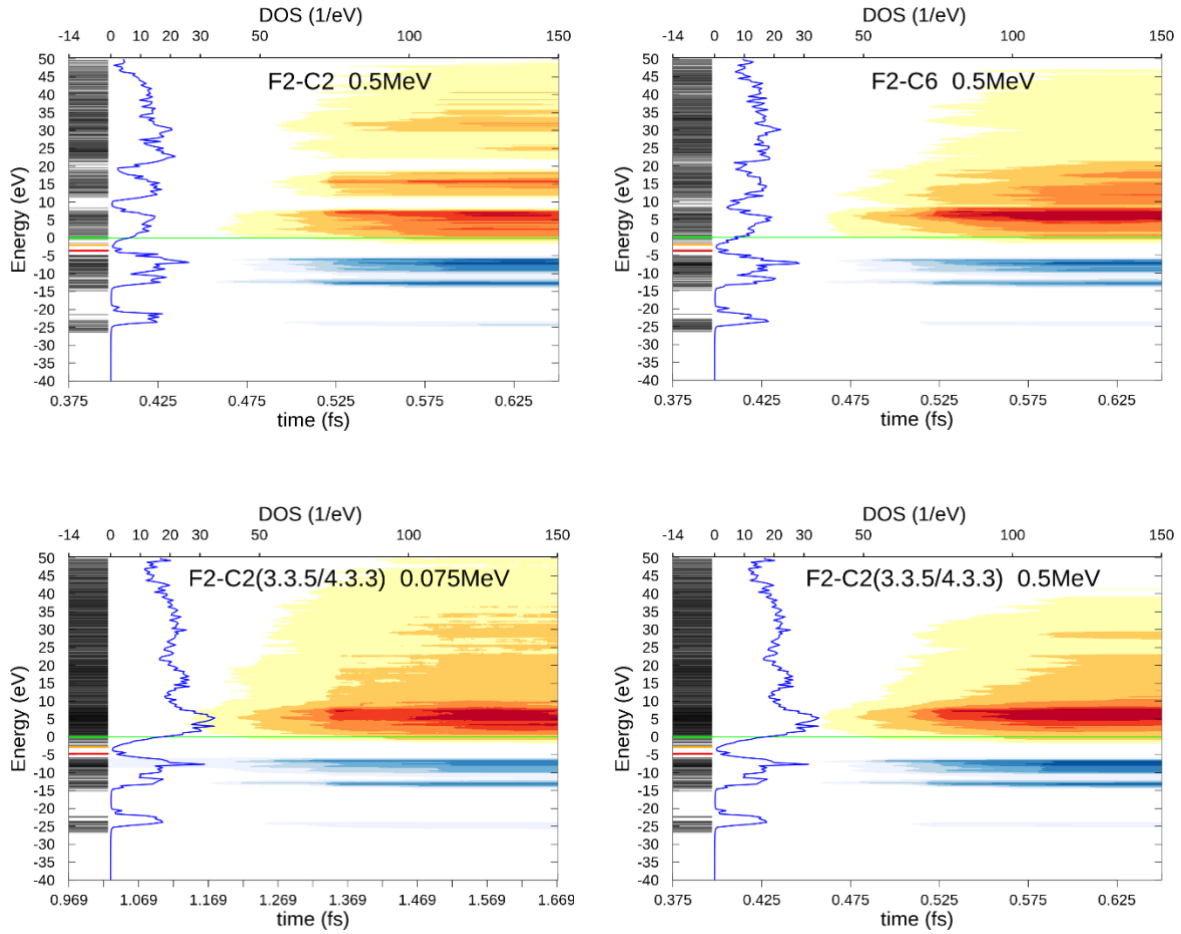

Figure 2: time evolution of the Kohn-Sham MO manifold with respect to the ground state for different basis sets and projectile's kinetic energies, for one water slab. Blue and orange colors respectively indicate depopulation and population of MO. The time window chosen to define the abscissa scale corresponds to the times for which the projectile is 5 Å before and after the water aggregate. The left-hand-side of each graph depicts the MO diagrams, highlining the HOMO, LUMO and zero energy levels with red, orange and green bars respectively. Finally, the vertical blue curves represent the density-of-state (DOS). See Fig. S1 for the other basis sets and kinetic energies.

2.4 Stopping power calculation

The total energy of a molecule/projectile system comprises the projectile kinetic energy, the molecular system energy and the projectile/molecule interaction energy, denoted as E_{kin}^{prj}, E^{mol} and $E^{mol/prj}$ respectively. The stopping power is defined as the loss of projectile's kinetic energy as it penetrates in matter, *i.e.* $S \equiv -\partial E_{kin}^{prj}/\partial r_{prj}$ or $S = \partial\left(E^{mol} + E^{mol/prj}\right)/\partial r_{prj}$. In our simulations, we fix the projectile's kinetic energy and we work within the frozen nuclei approximation. Hence, we directly obtain the electronic contribution S_e with the later expression. The sum of E^{mol} and $E^{mol/prj}$ is evaluated in the ADFT framework according to:

$$E^{mol} = E_{core}[\rho] + J[\rho, \tilde{\rho}] + E_{XC}[\tilde{\rho}] + E_{NR} \quad (3)$$

$$J[\rho, \tilde{\rho}] = \iint \frac{\rho(\boldsymbol{r_1})\tilde{\rho}(\boldsymbol{r_2})}{|\boldsymbol{r_1} - \boldsymbol{r_2}|} d\boldsymbol{r_1} d\boldsymbol{r_2} - \frac{1}{2} \iint \frac{\tilde{\rho}(\boldsymbol{r_1})\tilde{\rho}(\boldsymbol{r_2})}{|\boldsymbol{r_1} - \boldsymbol{r_2}|} d\boldsymbol{r_1} d\boldsymbol{r_2} \quad (4)$$

$$E^{mol/prj} = -\int \frac{\rho(\boldsymbol{r}) Z_{prj}}{|\boldsymbol{r} - \boldsymbol{R}_{prj}|} d\boldsymbol{r} + \sum_A \frac{Z_A Z_{prj}}{|\boldsymbol{R}_A - \boldsymbol{R}_{prj}|} \quad (5)$$

$$E^{ADFT} = E^{mol} + E^{mol/prj} \quad (6)$$

where E_{core} is the core electronic energy collecting electronic kinetic energy and Coulomb attraction with all atom nuclei, except for the projectile. J and E_{XC} are respectively the classical Coulomb repulsion and the exchange-correlation energies. J is calculated with the help of variational density fitting (Eq. 4)[56,57]. The fitted density ($\tilde{\rho}$) is also used to evaluate the XC energy and potentiall[49]. E_{NR} is the nuclear repulsion among atom nuclei. The first term on the right-hand side of Eq. 5 is the Coulomb attraction between electrons and the projectile, the charge and position vector of which are denoted Z_{prj} and $\boldsymbol{R}_{prj}$ respectively (vectors are written in bold). The second term is the repulsion between the projectile and the atom nuclei (A) with charge Z_A and position $\boldsymbol{R}_A$. Note that for finite system irradiation, $E^{mol/prj}$ vanishes when the projectile is far from the molecular system of interest. Figure 3 depicts typical energy profiles for two proton's kinetic energies, namely 0.075 MeV and 0.6 MeV. The black curves represent the variation of the ADFT energy with respect to the ground state energy. The origin of the projectile-molecule distance metric is set by convention to the moment when the projectile enters the van der Waals envelop of the molecule. Sharp energy rises are seen when the projectile-molecule distance reaches 3.1, 8.2 and 9 Å. These three peaks correspond to the passage of the projectile close to atomic nuclei. On the other hand, the red curves (ΔE^{mol}) are smoother. ΔE^{mol}can be regarded as the energy deposited into the electron cloud upon collision. The vertical dashed lines correspond to the entrance and exit of the projectile in the water slab.

The extraction of stopping power values from RT-TD-DFT simulations is not straightforward for disordered molecular systems and in absence of periodicity[19,28]. We have here considered four ways for evaluating S_e. We either take the overall energy variation between the entry and exit points that we divide by the distance travelled by the projectile ($S_e^{\Delta E}$), or we evaluate the instantaneous stopping power values at every propagation step and we average this quantity over the entire penetration period ($\langle S_e^{\delta E} \rangle$). The two approaches can be combined considering either the ΔE^{mol} or ΔE^{ADFT}energies. $S_e^{\Delta E}$ and $\langle S_e^{\delta E} \rangle$ are expected to give same values by construction within numerical rounding errors. This is indeed what we find for the two simulations showed on the Table 3. We find that considering the smoother ΔE^{mol} curves leads reliable estimates of S_e. This is the approach retained for the rest of this article ($S_e \equiv \langle S_e^{\delta E} \rangle$ with ΔE^{mol}).

Table 3: electronic stopping power in Ha/bohr calculated for one water slab with the four methods described in the text.

E_{kin}^{prj}		$\Delta E^{mol} + \Delta E^{mol/prj}$	ΔE^{mol}
0.075 MeV	$S_e^{\Delta E}$	0.229	0.235
	$\langle S_e^{\delta E} \rangle$	0.228	0.235
0.6 MeV	$S_e^{\Delta E}$	0.071	0.070
	$\langle S_e^{\delta E} \rangle$	0.071	0.069

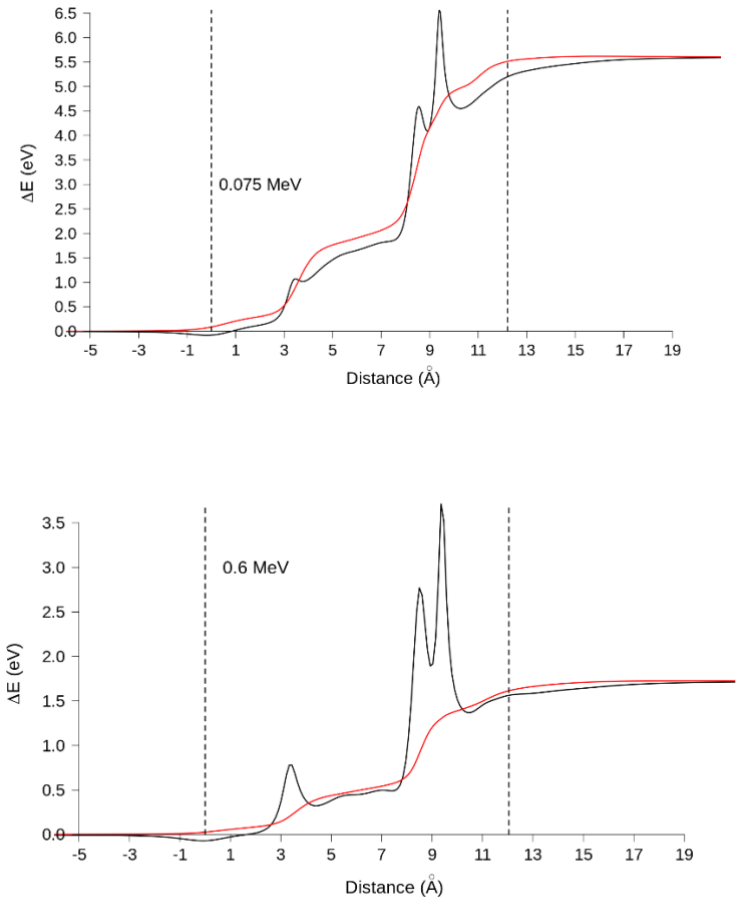

Figure 3: examples of energy profiles associated with the collision of a water slab by a 0.075 or 0.6 MeV proton. The black curve corresponds to the variation of ADFT energy (E^{ADFT}) while the red curve corresponds to the variation of E^{mol} as a function of the distance of the projectile with the water slab. The vertical dashed lines indicate when the projectile enters and exits the van der Waals envelope of the water slab, the former instant defining null distance.

2.5 Basis set benchmarks on water slabs

We explore in this section the influence of the basis set quality on the electronic stopping power average over 12 water slabs. For each projectile's kinetic energy, we independently ran 12 RT-TD-ADFT

simulations and calculated $\langle S_e^{\delta E} \rangle$ for each of them as detailed in the previous section. We report on the graphs the average over these 12 $\langle S_e^{\delta E} \rangle$ values. For each kinetic energy the statistical uncertainty is estimated via the Student law as $\pm 2.179 * \sqrt{u^2/12}$ where u^2 is the variance of the stopping power calculated over the 12 slabs. We start by considering the series of Dunning basis sets (Figure 4). A typical non-monotonic shape is obtained in each case, confirming the ability of RT-TD-ADFT to capture the physics at play in such irradiation. The standard deviations are significant, indicating the strong sensitivity of the S_e with the molecular geometry. In that regard, it should be noted that most curves largely overshoot the experimental curve which exhibits a value of 0.16 Ha/bohr at the Bragg peak[58]. This overestimation is the consequence of the projectile-water molecule distances sampled in the water slabs compared to the distribution that would be found for bulk water[19]. This is however not an issue for discussing basis set effects on S_e calculation. The geometry sampling issue will be addressed in section 3. For the present discussion, we consider that a higher S_e computed value would indicate better description of electronic excitation, hence better basis set. Coming back to Figure 4, the maximum of the curve, *i.e.* the so-called Bragg peak is not sensitive to basis set as soon as the F2-C3 basis set is used (cc-pVDZ on all atoms and cc-pVTZ on water$_{close}$ oxygens). On the other hand, the calculated electronic stopping power is strongly dependent on the basis set. Going through the F2-C2 to F4-C6 series leads to a seemingly continuous increase of S_e values. It is quite frustrating that even the rich, and computationally involved F4-C6 combination does not seem to ensure convergence. Nevertheless, when the expensive sextuple zeta basis set is used on water$_{close}$ oxygen atoms while keeping cc-pVDZ on all other atoms (F2-C6), we recover almost the same curve as F4-C6. This indicates that for the water systems investigated here, the quality of the basis set is a critical parameter for the atoms along the particle track, but not so much for the more remote atoms. One understands why small Dunning basis sets like F2-C2 and F2-C3 largely underestimates S_e looking at Figure 2. It is apparent that several excitations cannot take place upon irradiation because the DOS associated to these basis sets exibit holes (e.g. around 10 and 20 eV). One strategy to go toward the basis set limit would be to further enrich the basis set on hydrogen atoms or on water$_{far}$ molecules. A more systematic approach was proposed by Maliyov *et al*. [32] relying on a trial-and-error optimization algorithm to select the basis functions that most contribute to energy deposition. They applied this algorithm to S_e calculations in Li and Al. The approach leads to heavy basis sets which are computationally expensive to use, not to mention the need to optimize the basis set in preliminary simulations on smaller systems.

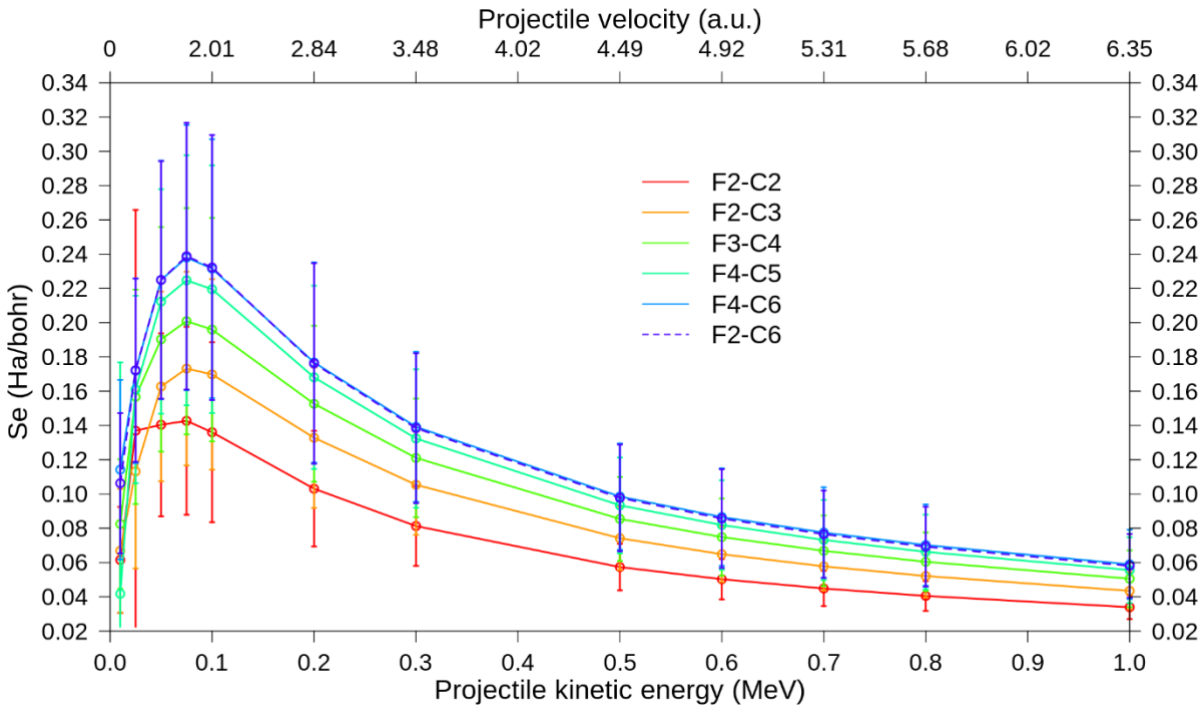

Figure 4: electronic stopping power for proton in water slabs as a function of the projectile kinetic energy with a series of Dunning standard basis sets (see Table 2). The error bars are the standard deviations calculated over the 12 water slabs with a confidence interval of 95%.

Actually, the poor convergence property of S_e depicted in Figure 4 suggests that increasing the degree of valence splitting is not the best strategy to follow. As stated in Introduction, we turn in this article to the use of AOC basis functions, that we add on top of the F2-C2 or F2-C3 basis set (Table 2) on water molecules lying within 2.6 Å of the projectile propagation line.

We start by comparing the F2-C2(3.2.5/3.2.5), F2-C3(3.2.5/3.2.5), F2-C2(3.3.5/3.2.5) and F2-C3(3.3.5/3.2.5) (Figure 5). The effect of adding AOC to the standard cc-pVDZ basis sets is substantial. Already with the F2-C2(3.2.5/3.2.5), the S_e curve approaches the one obtained for F4-C5. The improvement is spectacular around the Bragg peak (0.01 - 0.2 MeV) and even for high projectile kinetic energies the F2-C2(3.2.5/3.2.5) basis outperforms the F2-C2 basis set. The S_e curve obtained with F2-C2(3.2.5/3.2.5) confirms our intuition that improving the description of the continuum is crucial to obtain reliable S_e. The F2-C3(3.2.5/3.2.5) basis set helps to further increase the stopping power value, but it is when one increases L_{max} from 2 to 3 for AOC on oxygen that one gets significant increase. Interestingly, the combination of (3.3.5/3.2.5) with either F2-C2 or F2-C3 gives similar results indicating that when atomic orbitals for the continuum are used, a description of valence electrons by a simple double zeta basis set is good enough. Actually, the combination of (3.3.5/3.2.5) with the mininal STO-3G basis set (Fmin-Cmin(3.3.5/3.2.5)) gives a curve similar to that obtained with F2-C2(3.3.5/3.2.5) (Fig. S2). The region around the Bragg peak is well captured by standard basis sets enriched with the (3.3.5/3.2.5) AOC sets. On the other hand, for higher projectile's energy, a gap remains with S_e

calculated with F4-C6 (or F2-C6) and the choice of a given AOC set has little influence on this gap. To probe if lower energy states are populated for projectile kinetic energies above 0.2 MeV, we have run a series of calculation using a Dunning-Hay basis set[45] fitted to describe low energy Rydberg states and AOC (F2-Cryd2(3.3.5/3.2.5), Table 2). Results are showed in Fig. S2 and indicate no substantial differences with F2-C2(3.3.5/3.2.5) after the Bragg peak. In another test we have considered the addition of diffuse functions on the water$_{close}$ oxygens or moving to a quadruple level valence splitting (basis set combinations F2-Caug2(3.3.5/4.3.3) and F2-C4(3.3.5/4.3.3) respectively). The results are shown on in Fig. S3. First adding diffuse functions has no impact to the stopping power curves. On the other hand, comparing F2-C4(3.3.5/4.3.3) with F3-C4 shows, as before a remarkable improvement near the Bragg peak, and a slight improvement at higher energies, reducing the gap with F4-C6 or F2-C6. Actually, the examination of the excitation patterns (Fig. S1) reveals no major differences between F2-C6 and F2-C2(3.3.5/4.3.3), except at very high energy (> 40 eV), where the former basis sets affords more excitations. In principle this energy range is covered by the AOC we generated for this article, but one may add other sets of AOC parameters in the future to better describe this excitation domain.

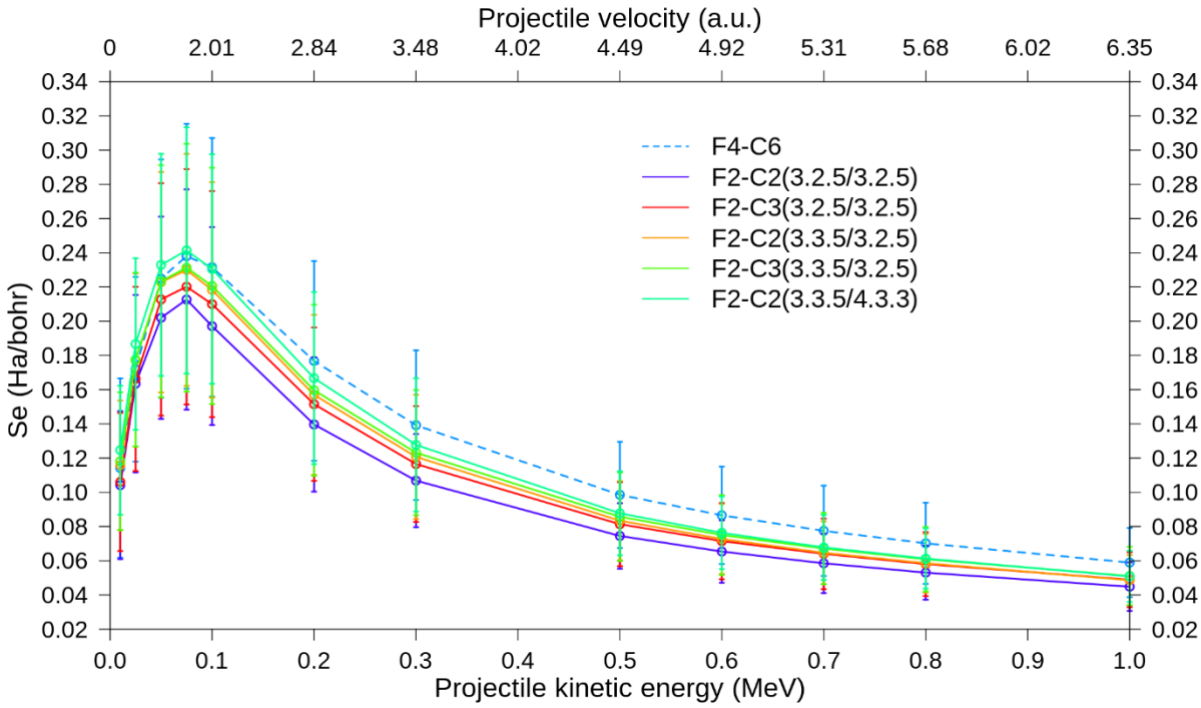

Figure 5: average electronic stopping power for proton penetrating water slabs as a function of the projectile kinetic energy with a Dunning standard basis set augmented by AOC (see Table 2). The error bars are the standard deviations calculated over the 12 water slabs with a confidence interval of 95%.

A further increase of L_{max} from 3 to 4 (F2-C2(3.4.5/3.2.5) *vs*. F2-C2(3.3.5/3.2.5)) leaves the S_e almost unchanged, but still slightly below the values provided by the F4-C6 basis set (Fig. S4). With F2-C2(3.3.5/4.3.3), AOC with L_{max} =3 are added on both hydrogen and oxygen atoms of the water$_{close}$ ensemble of molecules, the S_e curves are the largest near the Bragg peak and then slightly below the

S_e curves provided by F4-C6 at higher kinetic energies (Figure 5). Note that the F2-C2(3.3.5/4.3.3) combination gives better results than those provided by F2-C2(3.4.5/3.2.5) basis set combination. This tends to show that it is better to increase L_{max} consistently on all atoms rather than focusing only on heavy atoms.

The set comprised of F2-C2(3.2.5/3.2.5), F2-C2(8.2.5/8.2.5) and F2-C2(12.2.5/12.2.5) permits to evaluate the influence of the *R* parameter, which is respectively set it to 3, 8 or 12 bohr (Fig. S5). We see a small upward shift around the Bragg peak when going from F2-C2(3.2.5/3.2.5) to F2-C2(8.2.5/8.2.5), otherwise we see no much influence of the parameter for higher projectile kinetic energy. The curves obtained for F2-C2(8.2.5/8.2.5) and F2-C2(12.2.5/12.2.5) are almost superimposable. The *R* parameters seems to have less influence than the L_{max} parameter.

In another series of tests, we consider the F2-C2(3.2.5/3.2.5) but we vary the number of atoms on which this basis set is placed (Figure 6). With F2-C2(3.2.5/3.2.5)-b, only the oxygen atoms situated within 2 Å from the propagation line hold a (3.2.5/3.2.5) AOC set, not the hydrogen covalently linked to them. We see that the S_e curve significantly drops down, indicating that it is needed to have continuum basis functions on both oxygen and hydrogen atoms. With F2-C2(3.2.5/3.2.5)-c, a (3.2.5/3.2.5) AOC set is also positioned on oxygen atom situated 4 Å away from the projectile propagation line, and with F2-C2(3.2.5/3.2.5)-d is further enriched with (3.2.5/3.2.5) AOC set on the hydrogen atoms bonded to them. In both cases, the S_e curves are slightly modified. This is a result indicating that energy deposition is a very local property and the need to have dedicated basis set to describe the continuum is restricted to the atoms that are the closest from the propagation line, *i.e*. the atoms directly struck by the projectile.

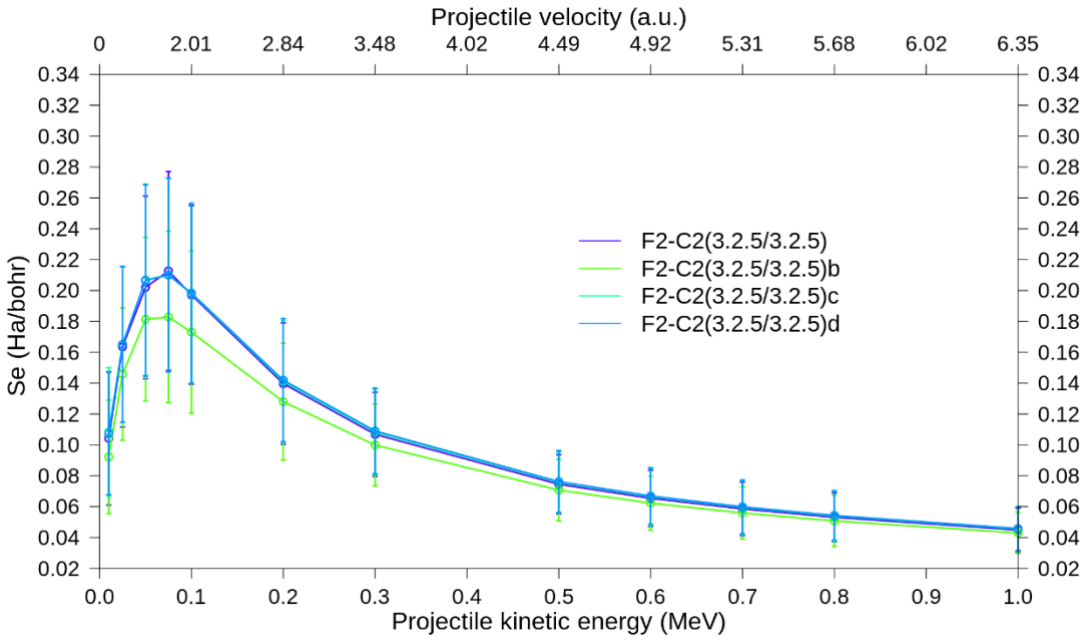

Figure 6: electronic stopping power for proton in water slabs as a function of the projectile kinetic energy with a Dunning standard basis set augmented by AOC placed on various atoms (see Table 2). The error bars are the standard deviations calculated over the 12 water slabs with a confidence interval of 95%.

2.5 Computational cost

The computational timings generated by all the basis sets are collected in Figure 7, taking the F2-C2 simulation as reference. The dashed line is a parabolic fit with the number of atomic orbitals. The overall trend is due to the Dunning cc-pV5Z and cc-pV6Z basis sets. Very satisfactorily, the advisable F2-C2(3.3.5/3.2.5) basis set is only 1.56 times more computationally expensive than the simple cc-pVDZ basis set. By comparison the F4-C6 basis set is 5 times more expensive. However, we showed that the F2-C6 basis set provides results of similar quality for a much lower computational cost (a ratio of 1.76 is found with F2-C2). Eventually, the use of a minimal basis set enriched with AOC (Fmin-Cmin(3.3.5/3.2.5)) may be a good solution if one is interested for instance in carrying out extensive sampling of impact parameters. Future work should address the relevance of this conclusion for other chemical systems containing not only oxygen or hydrogen atoms.

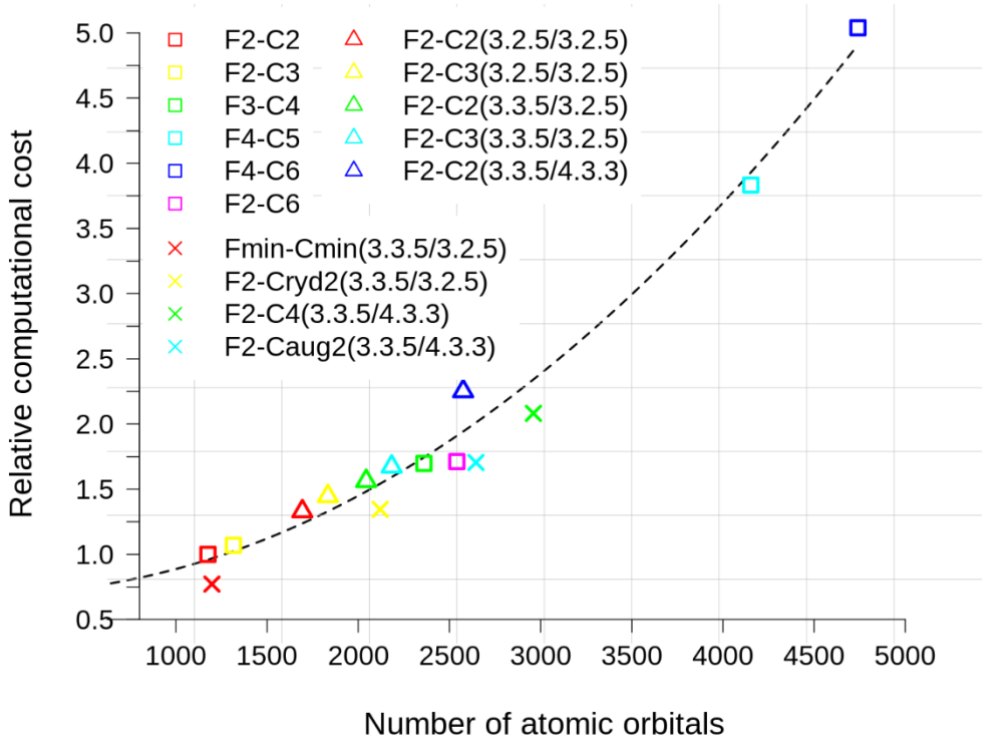

Figure 7: relative computational cost of RT-TD-ADFT simulations taking the F2-C2 basis set as reference. The dashed line is a parabolic fit over all data points. All the simulations have been run on the Adastra machine (CINES, France) with one node encompassing 8 GPU and 64 CPU.

3. Comparison with experimental stopping power

Having benchmarked Gaussian basis sets effects on average S_e values, we now move to comparison with experimental data. To this end, we consider a more realistic model than the gas phase water slab investigated in Section 2 (Figure 1). Indeed, to minimize border effect, we rely on a QM/MM (Quantum Mechanics /Molecular Mechanics) methodology[59]. In a first step we carried out a Langevin molecular dynamics simulation of a 100 Å^3 water box with the TIP3P model[60] at 298 K for 1 ns with the CHARMM program[61]. We first extracted 20 regularly-spaced-snapshots from the simulation and used them in subsequent RT-TD-ADFT/MM simulations. For each snapshot, the QM region was determined by defining a cylinder centered at the water box's center and aligned along the z-axis (Figure 8). The cylinder has radius and length of 6 and 16 Å respectively. Any water molecule the oxygen atom of which was contained in the cylinder's volume, was included in the QM region. On average the QM region encompassed 67 water molecules. For the stopping power calculation, we eliminated two 2.5 Å-length cylindrical layers at the extremities in order to alleviate border effect. To assess the convergence with basis set, we first conducted three series of simulations with the following basis set

combinations: F2-C2(3.3.5/4.3.3), F2-C4(3.3.5/4.3.3) and F2-Ccor2(3.3.5/4.3.3). All other simulation parameters were similar to those used for the water slabs (section 2.2).

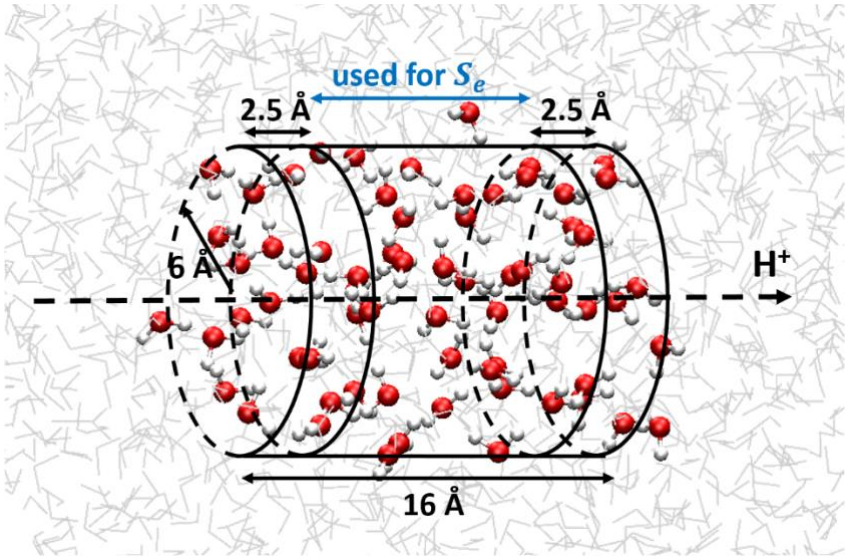

Figure 8: QM/MM set-up developed to evaluate the electronic stopping power. Water molecules described at the MM level are shown in grey sticks, while water molecules described at the DFT level are shown with ball-and-stick representation.

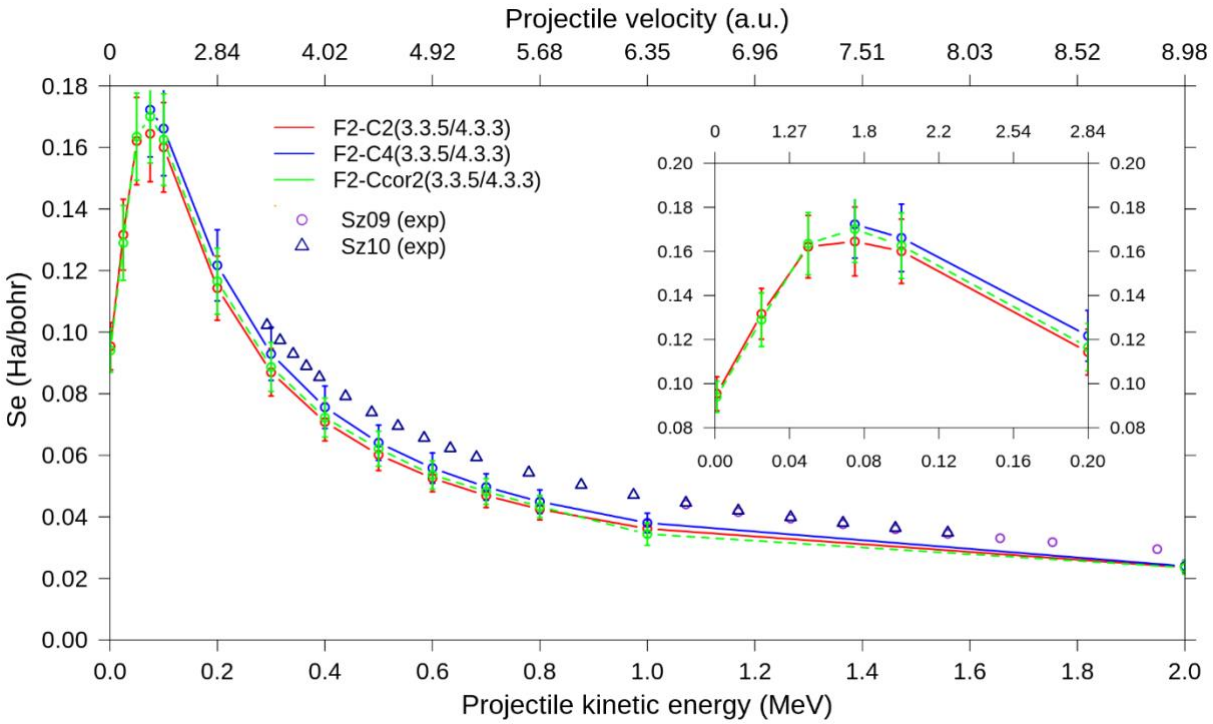

Figure 9: electronic stopping power obtained with our Gaussian Basis set RT-TD-ADFT approach using 20 QM/MM water cylinders. Comparison with experiments (Sz09 [62] and Sz10 [63]). Three basis sets are tested.

The simulated stopping power curves calculated at the RT-TD-ADFT level are shown in Figure 9. We also report the experimental measurements from Shimizu and coll. [62,63] A first striking observation is

the weak basis set sensitivity of the S_e curve. Comparing F2-C2(3.3.5/4.3.3) and F2-C4(3.3.5/4.3.3) indicates that going from cc-pVDZ to cc-pVQZ on the water$_{close}$ oxygens has a small impact. The blue curve lies slightly above the red one until 1 MeV. This result is in line with the previous benchmarks on water slabs (Fig. S3). When AOC are used, the valence splitting level has much less impact on energy deposition than when AOC are absent. The use of tight-core Dunning basis sets (green-dashed curve) has also little impact. Apart at the Bragg peak, the F2-C2(3.3.5/4.3.3) and F2-Ccor2(3.3.5/4.3.3) basis sets provide similar results. In summary, we conclude that our simulated S_e curves are converged with respect to the basis set. If we compare them to the available experimental data on the 0.29 to 1.94 MeV energy range, we note a systematic underestimation of the RT-TD-ADFT values.

Actually, a closer analysis of the 20 molecular geometries might provide an explanation of the discrepancy between our calculated curves and the experimental ones. Indeed, our set of geometries might not properly sample the distances between the irradiating ion and the atoms composing the system. Kohanoff and co-workers nicely demonstrated the importance of a proper sampling for such calculations[19]. The probability distributions of the minimum projectile-atom-distances differ somehow from ideal distributions (Fig. S6). Notably, this Figure shows that the 20 geometries do not sample projection-oxygen distances below 0.37 Å. To cure this issue, we first have extended our sets of geometries with 8 new configurations. These configurations were obtained taking one of the precedent geometries and shifting the projectile's impact parameter in the 0.05-0.37 Å window in order to more closely collide water molecules. Second, we have applied a reweighting procedure. Specifically, after the calculation of a given instantaneous stopping power value $S_e^{\delta E}$, we calculate the projectile-ion distance in order to determine a correcting weight. The latter is simply the ratio between the normalized probabilities. RT-TD-ADFT simulations with the F2-C2(3.3.5/4.3.3) basis set combination have been run on the supplementary systems.

Results are reported in Figure 10. We complement the graph with stopping power curves obtained with the SRIM (The Stopping and Range of Ions in Matter)[64] and PSTAR (Stopping Power and Range Tables for Protons)[58]. The stopping power curves obtained by Reeves et al. [65] and by Yao et al.[20] with a plane-wave RT-TD-DFT implementation are also reported for comparison. Considering first the brute RT-TD-ADFT data (no reweighting, red-dashed curve), we note that including 8 supplementary cylinders has a strong effect on the average S_e. At high kinetic energies, the calculated curve is slightly above the experimental one, but near the Bragg peak, it largely overshoots the semi-empirical SRIM and PSTAR curves. Clearly, the projectile-atom sampling quality is a major parameter impacting the average S_e. This parameter is actually as important as the basis set quality.

The reweighted RT-TD-ADFT stopping power curve, on the other hand, compares very well with the experiment and the SRIM and PSTAR models. Above 0.9 MeV, the RT-TD-ADFT curves lie very close to the experimental points and slightly below those provided by semi-empirical approaches. At the Bragg peak the agreement is also good with the semi-empirical models. For very low kinetic energy (0.01-0.05 MeV) our values overestimate those provided by the semi-empirical models. Electron attachment to the projectile at low velocities would reduce the effective charge of the projectile and decrease the stopping power. This could be an explanation of the overestimation that will deserve to be addressed more in depth.

The comparison with other TD-DFT calculations using plane-wave basis functions is also encouraging. The data reported in 2016 by Kanai co-worker (RYK16)[65] used a cutoff value of 50 Ry and the 1s electrons of oxygen atoms were treated as core electrons with a pseudopotential. With a more sophisticated protocol, with a 250 Ry cutoff and all electrons represented explicitly, this research group later obtained a better agreement with experimental data (YYK19)[20]. Here, our aim is to show that RT-TD-ADFT with Gaussian basis set can perform as good as a plane-wave code for electronic stopping power calculation provided adequate basis functions are used together with a proper configurational sampling. In that regard, it is delicate to push further the comparison between plane-wave and Gaussian basis sets curves as different sets of geometries have been used.

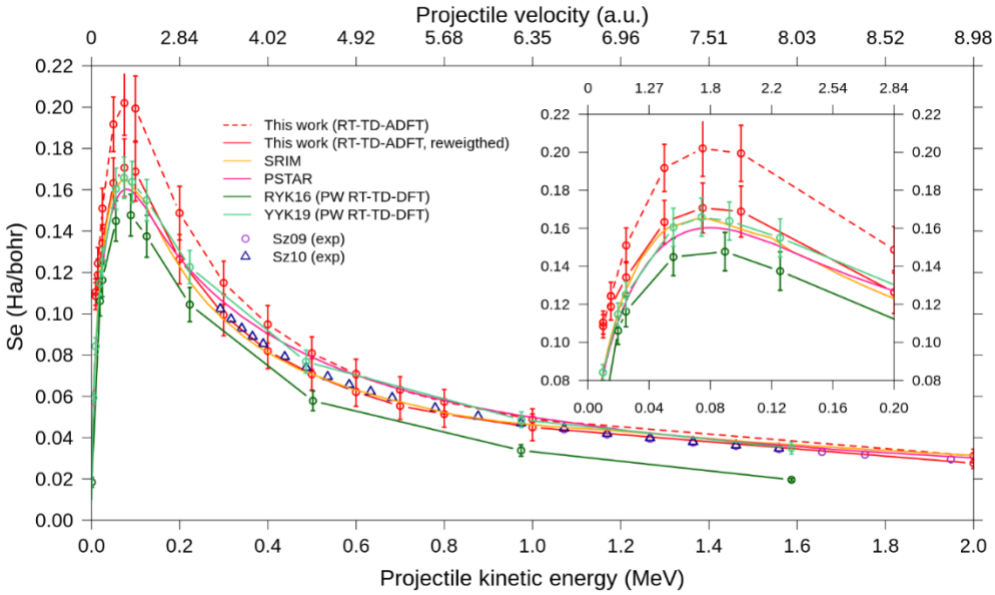

Figure 10: electronic stopping power obtained with our Gaussian Basis set RT-TD-ADFT approach using 29 QM/MM water cylinders. Comparison with experiments (Sz09 [62] and Sz10 [63]), semi-empirical models (SRIM and PSTAR) and with other plane-wave (PW) RT-TD-DFT implementation of Reeves et al. (RYK16) [65] and Yao et al. (YYK19)[20].

Conclusions

In this article, we have reported extensive benchmarks of RT-TD-ADFT electronic stopping power calculations with a code relying on atom-centered basis functions. The novelty of the present work was to investigate the relevance of Gaussian basis functions fitted to describe the continuum (AOC). We have considered liquid water models irradiated by protons in the 0.01-1 MeV kinetic energy range. We found that the addition of AOC on top of standard basis sets is very beneficial. AOC-augmented double-zeta basis sets were shown to give reliable electronic stopping power values. Even the combination of AOC with the minimal basis STO-3G basis set gave satisfactory results. The effect is mostly noticeable around the Bragg peak where electron transitions are the most energetic, but for faster projectiles, AOC still clearly improve S_e predictions. On the other hand the need to capture lower energy transitions puts pressure on the quality of valence electron description (and eventually also core excitations[31]). We found that AOC only need to be placed on the molecules that are most closely lying to the projectile's propagation track. Furthermore, the addition of AOC on these atoms makes superfluous the basis set enrichment on atoms positioned further away from this line. The consequence of these prescriptions is a very modest increase of the computational cost associated with the use of AOC (Figure 7). According to our benchmarks for water slabs irradiation by fast protons, it seems advisable to fit AOC with a rather small parameter extension ($R = 3$ bohr) and to opt for pronounced angular flexibility by setting the L_{max} quantum number to 3. We applied the optimal F2-C2(3.3.5/4.3.3) set-up to a QM/MM model for bulk water, which gave good agreement with experimental data. As already documented in Ref. 19, particular attention must be paid to properly sample projectile-atom distances or, as here to apply a reweighting procedure to obtain reliable average stopping power values. In summary, this first application of Gaussian AOC for the calculation of electronic stopping power opens the door for more extensive benchmarks, for example with other irradiating ions and/or for other materials.

Supporting Information

Tables of AOC developed for the present work. Density-of-state of the water molecule with Dunning basis set. Stopping power curves with minimal basis set and Dunning-Hay basis set augmented with AOC. Probability distribution of ion-atom nuclei distances for the QM/MM water cylinders. The data produced for this article and the Rstudio scripts written to generate most of the Figure can be downloaded on the Zenodo repository (DOI: 10.5281/zenodo.8037349)

Acknowledgements

We thank GENCI for generous computational resources (project number A0120806830), notably the CINES supercomputer and access to the newly released Adastra supercomputer via the Grand Challenge call. We are grateful toward Prof. Y. Kanai for providing us with their plane-wave RT-TD-DFT results for stopping power calculations. We thank the Agence Nationale de la Recherche (ANR project RUBI number: ANR-19-CE29-0011-01).

References

(1) Lacombe, S.; Porcel, E.; Scifoni, E. Particle Therapy and Nanomedicine: State of Art and Research Perspectives. *Cancer Nanotech.* **2017**, *8* (1), 9. https://doi.org/10.1186/s12645-017-0029-x.

(2) Indriolo, N.; McCall, B. J. Cosmic-Ray Astrochemistry. *Chem. Soc. Rev.* **2013**, *42* (19), 7763–7773. https://doi.org/10.1039/C3CS60087D.

(3) Grenier, I. A.; Black, J. H.; Strong, A. W. The Nine Lives of Cosmic Rays in Galaxies. *Annu. Rev. Astron. Astrophys.* **2015**, *53* (1), 199–246. https://doi.org/10.1146/annurev-astro-082214-122457.

(4) Cassidy, T.; Coll, P.; Raulin, F.; Carlson, R. W.; Johnson, R. E.; Loeffler, M. J.; Hand, K. P.; Baragiola, R. A. Radiolysis and Photolysis of Icy Satellite Surfaces: Experiments and Theory. *Space Science Reviews* **2010**, *153* (1), 299–315. https://doi.org/10.1007/s11214-009-9625-3.

(5) Bennett, C. J.; Pirim, C.; Orlando, T. M. Space-Weathering of Solar System Bodies: A Laboratory Perspective. *Chem. Rev.* **2013**, *113* (12), 9086–9150. https://doi.org/10.1021/cr400153k.

(6) Pomaro, B. A Review on Radiation Damage in Concrete for Nuclear Facilities: From Experiments to Modeling. *Modelling and Simulation in Engineering* **2016**, *2016*, 4165746. https://doi.org/10.1155/2016/4165746.

(7) Muñoz-Santiburcio, D.; Kohanoff, J.; Artacho, E. Electronic-Mediated Nuclear Stopping Power in Proton Irradiated Water Ice, 2023.

(8) Ziegler, J. F. Stopping of Energetic Light Ions in Elemental Matter. *J. Appl. Phys.* **1999**, *85* (3), 1249–1272. https://doi.org/10.1063/1.369844.

(9) Friedland, W.; Dingfelder, M.; Kundrát, P.; Jacob, P. Track Structures, DNA Targets and Radiation Effects in the Biophysical Monte Carlo Simulation Code PARTRAC. *Mutation Research/Fundamental and Molecular Mechanisms of Mutagenesis* **2011**, *711* (1–2), 28–40. http://dx.doi.org/10.1016/j.mrfmmm.2011.01.003.

(10) Kohn, W.; Sham, L. J. Self-Consistent Equations Including Exchange and Correlation Effects. *Phys. Rev.* **1965**, *140*, A1133–A1138. https://doi.org/10.1103/PhysRev.140.A1133.

(11) Hohenberg, P.; Kohn, W. Inhomogeneous Electron Gas. *Physical Review* **1964**, *136*, B864–B871. https://doi.org/10.1103/PhysRev.136.B864.

(12) Runge, E.; Gross, E. K. U. Density-Functional Theory for Time-Dependent Systems. *Phys. Rev. Lett.* **1984**, *52* (12), 997–1000.

(13) Li, X.; Govind, N.; Isborn, C.; DePrince, A. E.; Lopata, K. Real-Time Time-Dependent Electronic Structure Theory. *Chem. Rev.* **2020**, *120* (18), 9951–9993. https://doi.org/10.1021/acs.chemrev.0c00223.

(14) Omar, K. A.; Hasnaoui, K.; de la Lande, A. First-Principles Simulations of Biological Molecules Subjected to Ionizing Radiation. *Annu. Rev. Phys. Chem.* **2021**, *72* (1), 445–465. https://doi.org/10.1146/annurev-physchem-101419-013639.
(15) Johansson, J. O.; Henderson, G. G.; Remacle, F.; Campbell, E. E. B. Angular-Resolved Photoelectron Spectroscopy of Superatom Orbitals of Fullerenes. *Phys. Rev. Lett.* **2012**, *108* (17), 173401. https://doi.org/10.1103/PhysRevLett.108.173401.
(16) Yost, D. C.; Kanai, Y. Electronic Excitation Dynamics in DNA under Proton and α-Particle Irradiation. *J. Am. Chem. Soc.* **2019**, *141* (13), 5241–5251. https://doi.org/10.1021/jacs.8b12148.
(17) Alvarez-Ibarra, A.; Parise, A.; Hasnaoui, K.; de la Lande, A. The Physical Stage of Radiolysis of Solvated DNA by High-Energy-Transfer Particles: Insights from New First Principles Simulations. *Phys. Chem. Chem. Phys.* **2020**, *22* (15), 7747–7758. https://doi.org/10.1039/D0CP00165A.
(18) Pruneda, J. M.; Sánchez-Portal, D.; Arnau, A.; Juaristi, J. I.; Artacho, E. Electronic Stopping Power in LiF from First Principles. *Phys. Rev. Lett.* **2007**, *99* (23), 235501. https://doi.org/10.1103/PhysRevLett.99.235501.
(19) Gu, B.; Cunningham, B.; Muñoz Santiburcio, D.; Da Pieve, F.; Artacho, E.; Kohanoff, J. Efficient Ab Initio Calculation of Electronic Stopping in Disordered Systems via Geometry Pre-Sampling: Application to Liquid Water. *J. Chem. Phys.* **2020**, *153* (3), 034113. https://doi.org/10.1063/5.0014276.
(20) Yao, Y.; Yost, D. C.; Kanai, Y. K-Shell Core-Electron Excitations in Electronic Stopping of Protons in Water from First Principles. *Phys. Rev. Lett.* **2019**, *123* (6), 066401. https://doi.org/10.1103/PhysRevLett.123.066401.
(21) Shepard, C.; Yost, D. C.; Kanai, Y. Electronic Excitation Response of DNA to High-Energy Proton Radiation in Water. *Phys. Rev. Lett.* **2023**, *130* (11), 118401. https://doi.org/10.1103/PhysRevLett.130.118401.
(22) Bi, G.; Kang, J.; Wang, L.-W. High Velocity Proton Collision with Liquid Lithium: A Time Dependent Density Functional Theory Study. *Phys. Chem. Chem. Phys.* **2017**, *19* (13), 9053–9058. https://doi.org/10.1039/c7cp00132k.
(23) Correa, A. A. Calculating Electronic Stopping Power in Materials from First Principles. *Computat Mat Sci* **2018**, *150*, 291–303. https://doi.org/10.1016/j.commatsci.2018.03.064.
(24) A. Schleife; E. W. Draeger; V. M. Anisimov; A. A. Correa; Y. Kanai. Quantum Dynamics Simulation of Electrons in Materials on High-Performance Computers. *Comput. Scien. Eng.* **2014**, *16* (5), 54–60. https://doi.org/10.1109/mcse.2014.55.
(25) Quashie, E. E.; Correa, A. A. Electronic Stopping Power of Protons and Alpha Particles in Nickel. *Phys. Rev. B* **2018**, *98* (23), 235122. https://doi.org/10.1103/PhysRevB.98.235122.
(26) Schleife, A.; Kanai, Y.; Correa, A. A. Accurate Atomistic First-Principles Calculations of Electronic Stopping. *Phys. Rev. B* **2015**, *91* (1), 014306. https://doi.org/10.1103/PhysRevB.91.014306.
(27) Yost, D. C.; Yao, Y.; Kanai, Y. Examining Real-Time Time-Dependent Density Functional Theory Nonequilibrium Simulations for the Calculation of Electronic Stopping Power. *Phys. Rev. B* **2017**, *96* (11), 115134.
(28) Reeves, K. G.; Kanai, Y. Electronic Excitation Dynamics in Liquid Water under Proton Irradiation. *Sci. Rep.* **2017**, *7*, 40379. https://doi.org/10.1038/srep40379.
(29) Zeb, M. A.; Kohanoff, J.; Sánchez-Portal, D.; Artacho, E. Electronic Stopping Power of H and He in Al and LiF from First Principles. *Nuc Instr Meth Phys Res Sect B: Beam Interact Mat Atoms* **2013**, *303*, 59–61. https://doi.org/10.1016/j.nimb.2012.12.022.

(30) Zeb, M. A.; Kohanoff, J.; Sánchez-Portal, D.; Arnau, A.; Juaristi, J. I.; Artacho, E. Electronic Stopping Power in Gold: The Role of d Electrons and the H/He Anomaly. *Phys. Rev. Lett.* **2012**, *108* (22), 225504. https://doi.org/10.1103/PhysRevLett.108.225504.
(31) Maliyov, I.; Crocombette, J.-P.; Bruneval, F. Electronic Stopping Power from Time-Dependent Density-Functional Theory in Gaussian Basis. *Eur. Phys. J. B* **2018**, *91* (8), 172. https://doi.org/10.1140/epjb/e2018-90289-y.
(32) Maliyov, I.; Crocombette, J.-P.; Bruneval, F. Quantitative Electronic Stopping Power from Localized Basis Set. *Phys. Rev. B* **2020**, *101* (3), 035136. https://doi.org/10.1103/PhysRevB.101.035136.
(33) Labeye, M.; Zapata, F.; Coccia, E.; Véniard, V.; Toulouse, J.; Caillat, J.; Taïeb, R.; Luppi, E. Optimal Basis Set for Electron Dynamics in Strong Laser Fields: The Case of Molecular Ion H2+. *J. Chem. Theory Comput.* **2018**, *14* (11), 5846–5858. https://doi.org/10.1021/acs.jctc.8b00656.
(34) K Kaufmann; W Baumeister; M Jungen. Universal Gaussian Basis Sets for an Optimum Representation of Rydberg and Continuum Wavefunctions. *Journal of Physics B: Atomic, Molecular and Optical Physics* **1989**, *22* (14), 2223. https://doi.org/10.1088/0953-4075/22/14/007.
(35) Woźniak, A. P.; Lesiuk, M.; Przybytek, M.; Efimov, D. K.; Prauzner-Bechcicki, J. S.; Mandrysz, M.; Ciappina, M.; Pisanty, E.; Zakrzewski, J.; Lewenstein, M.; Moszyński, R. A Systematic Construction of Gaussian Basis Sets for the Description of Laser Field Ionization and High-Harmonic Generation. *J. Chem. Phys.* **2021**, *154* (9), 094111. https://doi.org/10.1063/5.0040879.
(36) B M Nestmann; S D Peyerimhoff. Optimized Gaussian Basis Sets for Representation of Continuum Wavefunctions. *J. Phys. B: At., Mol. Opt. Phys.* **1990**, *23* (22), L773. https://doi.org/10.1088/0953-4075/23/22/007.
(37) Faure, A.; Gorfinkiel, J. D.; Morgan, L. A.; Tennyson, J. GTOBAS: Fitting Continuum Functions with Gaussian-Type Orbitals. *Comput. Phys. Commu.* **2002**, *144* (2), 224–241. https://doi.org/10.1016/S0010-4655(02)00141-8.
(38) Jonathan Tennyson; Daniel B Brown; James J Munro; Iryna Rozum; Hemal N Varambhia; Natalia Vinci. Quantemol-N: An Expert System for Performing Electron Molecule Collision Calculations Using the R-Matrix Method. *J. Phys.: Conf. Series* **2007**, *86* (1), 012001. https://doi.org/10.1088/1742-6596/86/1/012001.
(39) Laporta, V.; Celiberto, R.; Tennyson, J. Dissociative Electron Attachment and Electron-Impact Resonant Dissociation of Vibrationally Excited O2 Molecules. *Phys. Rev. A* **2015**, *91* (1), 012701. https://doi.org/10.1103/PhysRevA.91.012701.
(40) Bouchiha, D.; Gorfinkiel, J. D.; Caron, L. G.; Sanche, L. Low-Energy Electron Collisions with Tetrahydrofuran. *J. Phys. B: At., Mol. Opt. Phys.* **2006**, *39* (4), 975. https://doi.org/10.1088/0953-4075/39/4/021.
(41) Morassut, C.; Luppi, E.; Coccia, E. A TD-CIS Study of High-Harmonic Generation of Uracil Cation Fragments. *Chem. Phys.* **2022**, *559*, 111515. https://doi.org/10.1016/j.chemphys.2022.111515.
(42) Dunning, T. H. Gaussian Basis Sets for Use in Correlated Molecular Calculations. I. The Atoms Boron through Neon and Hydrogen. *J. Chem. Phys.* **1989**, *90* (2), 1007–1023. https://doi.org/doi:http://dx.doi.org/10.1063/1.456153.
(43) Wilson, A. K.; van Mourik, T.; Dunning, T. H. Gaussian Basis Sets for Use in Correlated Molecular Calculations. VI. Sextuple Zeta Correlation Consistent Basis Sets for Boron through Neon. *J. Mol. Struc-THEOCHEM* **1996**, *388*, 339–349. https://doi.org/10.1016/s0166-1280(96)80048-0.

(44) Dunning, T. H. Gaussian Basis Functions for Use in Molecular Calculations. I. Contraction of (9s5p) Atomic Basis Sets for the First-Row Atoms. *J. Chem. Phys.* **1970**, *53*, 2823–2833. https://doi.org/10.1063/1.1674408.
(45) Dunning, T. H.; Hay, P. J. Gaussian Basis Sets for Molecular Calculations. In *Methods of Electronic Structure Theory*; Schaefer, H. F., Ed.; Modern Theoretical Chemistry; Springer, 1977; Vol. 3, pp 1–27. https://doi.org/10.1007/978-1-4757-0887-5.
(46) Pritchard, B. P.; Altarawy, D.; Didier, B.; Gibson, T. D.; Windus, T. L. New Basis Set Exchange: An Open, Up-to-Date Resource for the Molecular Sciences Community. *J. Chem. Inf. Model.* **2019**, *59* (11), 4814–4820. https://doi.org/10.1021/acs.jcim.9b00725.
(47) Martínez, Pablo Antonio; Vock, Theresa; Kharchi , Liliane Racha; Pedroza-Montero, J. N.; Hasnaoui, K.; de la Lande, Aurélien, A. A Multi-GPU Implementation of Real-Time Time-Dependent Auxiliary Density Functional Theory for the Investigation of Nanosystems Irradiations. *Computer Physics Communications under review*.
(48) Alvarez-Ibarra, A.; Köster, A. M. A New Mixed Self-Consistent Field Procedure. *Mol. Phys.* **2015**, *113* (19–20), 3128–3140. https://doi.org/10.1080/00268976.2015.1078009.
(49) Köster, A. M.; Reveles, J. U.; del Campo, J. M. Calculation of Exchange-Correlation Potentials with Auxiliary Function Densities. *J. Chem. Phys.* **2004**, *121* (8), 3417–3424. https://doi.org/doi:http://dx.doi.org/10.1063/1.1771638.
(50) Alvarez-Ibarra, A.; Omar, K. A.; Hasnaoui, K.; de la Lande, A. Chapter 4 Electron and Molecular Dynamics Simulations with Polarizable Embedding. In *Multiscale Dynamics Simulations: Nano and Nano-bio Systems in Complex Environments*; The Royal Society of Chemistry, 2022; pp 117–143. https://doi.org/10.1039/9781839164668-00117.
(51) Omar, K. A.; Korsaye, F. A.; Tandiana, R.; Tolu, D.; Deviers, J.; Wu, X.; Parise, A.; Alvarez-Ibarra, A.; Moncada, F.; Pedroza-Montero, J. N.; Mejia-Rodriguez, D.; Van-Oanh, N.-T.; Cailliez, F.; Clavaguera, C.; Hasnaoui, K.; de La Lande, A. Current Status of deMon2k to Simulate the Early Stages of Matter Subjected to High Energy Radiation. *Eur. Phys. J. S. T.* **2023**. https://doi.org/10.1140/epjs/s11734-023-00905-6.
(52) Tandiana, R.; Clavaguéra, C.; Hasnaoui, K.; Pedroza-Montero, J. N.; de la Lande, A. Reliability and Performances of Real-Time Time-Dependent Auxiliary Density Functional Theory. *Theor. Chem. Acc.* **2021**, *140* (9), 126–138. https://doi.org/10.1007/s00214-021-02819-9.
(53) Wu, X.; Alvarez-Ibarra, A.; Salahub, D. R.; de la Lande, A. Retardation in Electron Dynamics Simulations Based on Time-Dependent Density Functional Theory. *Eur. Phys. J. D* **2018**, *72* (12), 206. https://doi.org/10.1140/epjd/e2018-90219-3.
(54) Cheng, C.-L.; Evans, J. S.; Van Voorhis, T. Simulating Molecular Conductance Using Real-Time Density Functional Theory. *Phys. Rev. B* **2006**, *74* (15), 155112.
(55) R Core Team. *R: A Language and Environment for Statistical Computing*; R Foundation for Statistical Computing: Vienna, Austria, 2013.
(56) Dunlap, B. I.; Rösch, N.; Trickey, S. B. Variational Fitting Methods for Electronic Structure Calculations. *Mol. Phys.* **2010**, *108* (21–23), 3167–3180. https://doi.org/10.1080/00268976.2010.518982.
(57) Mejía-Rodríguez, D.; Trickey, S. B. Variational Properties of Auxiliary Density Functionals. *Theor. Chem. Acc.* **2021**, *140* (4), 37. https://doi.org/10.1007/s00214-021-02731-2.
(58) Berger, M. J.; Coursey, J. S.; Zucker, M. A.; Chang, J. ESTAR, PSTAR, and ASTAR: Computer Programs for Calculating Stopping-Power and Range Tables for Electrons, Protons, and Helium Ions, 2015.
(59) de la Lande, A.; Alvarez-Ibarra, A.; Hasnaoui, K.; Cailliez, F.; Wu, X.; Mineva, T.; Cuny, J.; Calaminici, P.; López-Sosa, L.; Geudtner, G.; Navizet, I.; Garcia Iriepa, C.;

Salahub, D. R.; Köster, A. M. Molecular Simulations with In-deMon2k QM/MM, a Tutorial-Review. *Molecules* **2019**, *24* (9), 1653.
(60) Sokalski, W. A.; Poirier, R. A. Cumulative Atomic Multipole Representation of the Molecular Charge Distribution and Its Basis Set Dependence. *Chem. Phys. Lett.* **1983**, *98* (1), 86–92. http://dx.doi.org/10.1016/0009-2614(83)80208-5.
(61) B. R. Brooks; C. L. Brooks III; A. D. Mackerell Jr; L. Nilsson; R. J. Petrella; B. Roux; Y. Won; G. Archontis; C. Bartels; S. Boresch; A. Caflisch; L. Caves; Q. Cui; A. R. Dinner; M. Feig; S. Fischer; J. Gao; M. Hodoscek; W. Im; K. Kuczera; T. Lazaridis; J. Ma; V. Ovchinnikov; E. Paci; R. W. Pastor; C. B. Post; J. Z. Pu; M. Schaefer; B. Tidor; R. M. Venable; H. L. Woodcock; X. Wu; W. Yang; D. M. York; M. Karplus. CHARMM: The Biomolecular Simulation Program. *J. Comput. Chem.* **2009**, *30* (10), 1545–1614.
(62) Shimizu, M.; Kaneda, M.; Hayakawa, T.; Tsuchida, H.; Itoh, A. Stopping Cross Sections of Liquid Water for MeV Energy Protons. *Nuc Instr Meth Phys Res Sect B: Beam Interact Mat Atoms* **2009**, *267* (16), 2667–2670. https://doi.org/10.1016/j.nimb.2009.05.036.
(63) Shimizu, M.; Hayakawa, T.; Kaneda, M.; Tsuchida, H.; Itoh, A. Stopping Cross-Sections of Liquid Water for 0.3–2.0 MeV Protons. *Vacuum* **2010**, *84* (8), 1002–1004. https://doi.org/10.1016/j.vacuum.2009.11.019.
(64) Ziegler, J. F.; Ziegler, M. D.; Biersack, J. P. SRIM – The Stopping and Range of Ions in Matter (2010). *Nuclear Instruments and Methods in Physics Research Section B: Beam Interactions with Materials and Atoms* **2010**, *268* (11), 1818–1823. https://doi.org/10.1016/j.nimb.2010.02.091.
(65) Reeves, K. G.; Yao, Y.; Kanai, Y. Electronic Stopping Power in Liquid Water for Protons and Alpha Particles from First Principles. *Phys. Rev. B* **2016**, *94* (4), 041108. https://doi.org/10.1103/PhysRevB.94.041108.